Numerical Methods in Civil Engineering, 10-3 (2026) 92-108

Numerical Methods in Civil Engineering

Journal Homepage: https://nmce.kntu.ac.ir/

Automated Detection of Pavement Fatigue Cracks with Deep Learning

Shaghayegh Alipour [*], ***Mojtaba Khodadadi*** [**], ***Mohammad Javad Amani*** [***], ***Ali Khodaii*** [***], ***Saeid Hesami*** [*]

ARTICLE INFO

RESEARCH PAPER

Article history:
Received:
November 2025
Revised:
February 2026
Accepted:
May 2026

Keywords:
Fatigue Cracks, Ground-Penetrating Radar, YOLO, Transfer Learning, Faster R-CNN.

Abstract:

This study uses advanced imaging techniques and deep learning algorithms to assess fatigue cracks through cyclic loading on asphalt specimens. Faster Region-Based Convolutional Neural Network (Faster R-CNN) and the You Only Look Once (YOLO) models were compared to detect fatigue cracks in Ground-Penetrating Radar (GPR) and Computed Tomography (CT) scan images and to detect concealed cracks in GPR field data. Crack detection was improved using transfer learning with pre-trained weights from the COCO dataset. Using the piecewise function model, the accumulative horizontal strain was accurately estimated. Based on the statistical analysis, the model's accuracy was verified, with no significant differences between experimental and predicted results. Moreover, a piecewise function applied to CT scan data resulted in a better understanding of fatigue behavior. The crack classification was improved after retraining pre-trained deep convolutional neural networks (PDCNNs). The YOLO models outperformed Faster-RCNN in terms of average precision. Models YOLOv7, YOLOv5s, and YOLOv8 performed well on the GPR dataset, while YOLOv5s, YOLOv5m, and YOLOv8 were the most effective models on the CT dataset.

1. Introduction

Flexible pavement cracks are primarily caused by fatigue phenomenon, which are common structural degradations. Adding accumulated load to the pavement surface causes micro and macro cracks to form and propagate over time [1]. To minimize the costs associated with pavement maintenance, it is crucial to accurately assess durability and predict lifespan of roads. Despite this, determining the fatigue properties of asphalt mixtures can be challenging and time-consuming. Understanding the fatigue behavior of mixture can assist in distinguishing between long-lasting and short-lasting pavement constructions [2,3].

Ground Penetrating Radar is widely used to inspect the subsurface of pavements. Besides its efficiency and low operating costs, this method is also time-saving and interference-resistant [4].

* *Corresponding Author: Department of Civil Engineering, Babol Noshirvani University of Technology, Mazandaran, Iran, 4714871167, E-mail: Sh.alipour20@gmail.com, s.hesami@nit.ac.ir*
** *Faculty of Civil Engineering at K. N. Toosi University of Technology, Tehran, Iran, 158754416, E-mail: M.khodadadi@kntu.ac.ir.*
*** *Department of Civil and Environmental Engineering, Amirkabir University of Technology (Tehran Polytechnic), Tehran, Iran, 1591634311, E-mail: {mjavad.Amani, Khodaii}@aut.ac.ir.*

In pavement inspection, it has been used to detect voids, pavement thickness variations, and buried utilities [5]. Although GPR technology has its advantages, it also has its limitations, for instance, the data must be post processed using complementary techniques and technologies. For a deeper understanding of the data collected from GPR, further analysis and interpretation may be required. It is possible to improve the accuracy and reliability of GPR surveys through the integration of other technologies, such as electromagnetic induction or seismic methods [6]. In addition, GPR data interpretation often requires experienced personnel to manually identify and analyze subsurface anomalies. Despite advances in automated algorithms and machine learning (ML) techniques for GPR data processing, it remains difficult to achieve reliable and efficient automatic detection [7–9]. A range of researches has been conducted to address these challenges and improve the effectiveness of GPR in pavement inspections, including development of advanced data processing algorithms, artificial intelligence-based approaches, and integrated multi-sensor systems [10].

Asphalt pavement cracking patterns have been identified by GPR over the past few years. To detect cracks and estimate

https://doi.org/10.61882/NMCE.2511.1110

crack widths, researchers explored various methods and techniques for manually processing GPR data [11]. The signal processing techniques used by Fernandes et al. [12] to detect single millimeter cracks in asphalt samples. They predicted crack width based on the amplitude of the reflected GPR signal, considering the permittivity contrast between adjacent layers. Furthermore, they used modeling software to verify their findings. As Rasol et al.[13] demonstrated, the relative amplitude measured at the hyperbola vertex corresponds to the width of a concealed crack in a laboratory rigid pavement overlaid with asphalt. To validate the results, numerical modeling was employed. However, accuracy was affected by the number of coring samples. In another approach, Solla et al. [14] combined GPR with infrared thermometers to quantitatively identify cracks in pavements. The study did not provide precise characteristics of these cracks although the cracks were mainly visible on the surface and not concealed. All of the studies mentioned above classified defects using GPR images manually.

A number of researchers have explored automated or semi-automated approaches to identifying defects in GPR images to overcome the limitations of manual classification. Convolutional neural networks (CNNs) are used in a study of Tong et al. [15] to automate recognition, location, measurement, and 3D reconstruction of concealed cracks using GPR. Using GPR and network-in-network structures, Tong et al. [16] distinguished abnormal signals, recognized distress types, and measured their sizes and locations. Training, validation, and testing are carried out by using a GPR database of four highways with varying transmitting frequencies and sample traces. In a study by Gao et al. [17] with the aim of increasing the accuracy and generalization of GPR-based pavement distress detection, Faster R-ConvNet models were trained, validated, and tested on GPR images while the stability and real-time capabilities of the model were demonstrated. With GPR, a mask region-based convolutional neural network (RCNN) is employed in a study by Liu et al. [18] to detect and segment cracks at the pixel level automatically. Using simulation software and field detection, crack features and the width-area relationship in GPR images were determined. In this study [19], Li et al. used 3-D GPR and You Only Look Once (YOLO) models to detect concealed cracks in asphalt pavement. YOLOv4 and YOLOv5 show significant improvements in detection even in a small dataset. According to Liu et al. [20], with GPR dataset, a YOLOv3 model with four detection layers improves detection accuracy, particularly for small crack features, whereas the YOLOv3-FDL model achieves better scores than YOLOv3. The use of advanced ML techniques led to an improvement in crack detection in the pavement, particularly Faster R-CNN and YOLO due to their speed and accuracy. For the following steps to be implemented, it is necessary to conduct further research regarding the type of cracks, such as fatigue cracks, and their pattern so as to gain a deeper understanding of pavement subsurface and find ways for pavements to be maintained in a more efficient manner. In recent years, crack detection has been improved with image processing and the integration of multiple sensing technologies such as CT scan, which shows promise for improving crack detection and classification.

According to Papagiannakis et al. [21] CT scans were used to study asphalt mixtures for their air void density and distribution, thereby improving understanding of how the material performs under traffic loads. The fracture behavior of asphalt mixtures, including crack initiation and propagation mechanisms, was studied using CT imaging by Saadeh et al. [22] to gain insight into the material's structural response through CT imaging. In a study by Banta et al. [23], CT scanning techniques were applied to assess the air void distribution and compaction characteristics of asphalt mixtures, resulting in insights into how compaction affects material properties. Wang et al. [24] used CT imaging to determine the effects of aggregate properties, gradation, and compaction methods on the internal structure and performance of asphalt mixtures. In a study by Khan et al. [25], laboratory fatigue tests were conducted on asphalt mixtures by varying temperatures and performing tension-compression cyclic tests. Three-dimensional images were generated by CT scanning at specific intervals in the testing process. Gao et al. [26] investigated air void characteristics in cold in-place recycled mixture specimens using CT and digital image processing, comparing the superpave gyratory and the static load compaction. In a study carried out by Hu et al. [27], to assess fatigue damage in asphalt mixtures, digital image processing was used to analyze microstructural changes in the internal composition and CT was used to scan internal structures before and after fatigue damage. According to Barroso et al. [28], CT was used to track crack evolution during fatigue tests using diametrical compression on asphalt mixtures. In a study by Li et al. [29], an advanced repeated load permanent deformation test was performed on asphalt mixtures, using CT and digital image processing to study microstructure evolution and damage during and after high temperature testing. According to Li et al. [30], a comparison of field and laboratory compaction methods for asphalt mixtures was carried out, as well as an analysis of void distribution, particle size, and aggregate degradation using X-ray CT and digital image processing. It is evident from the previous studies that CT scanning techniques can be used to characterize the internal structure, microstructure properties, void distribution, compaction characteristics, and performance of asphalt concrete materials, yet in all of the above studies; machine-learning methods were not utilized to automatically detect pavement features.

As a result of CT scanning's high precision and GPR's rapid data acquisition, fatigue cracks in asphalt samples consisting of two layers and subjected to fatigue loading and field data are detected in this study using GPR and CT scan (as a comparative method). The data obtained from CT scanning and GPR will be processed using YOLO and Faster RCNN with the help of some techniques such as transfer learning, followed by a comparison of fatigue test results with CT scan results. In the next phase, the performance of the YOLO and Faster RCNN programs based on the input data from CT scanning and GPR techniques will be compared in terms of crack detection accuracy. The GPR technique will be compared with the CT scan technique to assess the agreement between their results. In contrast to previous studies that focus independently on fatigue testing, CT-based damage characterization, or deep learning-based crack detection, this study introduces a fatigue-informed, multi-modal assessment framework for asphalt pavements. The specific innovations of this research include: (i) quantitative linkage of mechanically defined fatigue stages (t_{st} and FN) with CT-derived crack density evolution, enabling physical interpretation of internal crack development; (ii) validation of GPR-based concealed crack detection using CT imaging as a high-resolution reference; and (iii) systematic benchmarking of state-of-the-art deep learning object detection models across both CT and GPR datasets to enable automated, scalable, and fatigue-consistent crack assessment. These contributions collectively bridge laboratory-scale fatigue characterization and field-scale non-destructive pavement evaluation. Accordingly, the objective of this study is not limited to fatigue characterization or algorithm comparison alone, but rather to develop an integrated framework that links mechanical fatigue behavior, internal damage evolution, and non-destructive imaging through automated deep learning-based crack detection. Fatigue testing provides physically meaningful damage stages, CT scanning serves as a high-resolution reference for internal crack evolution, and GPR represents a practical field-deployable NDT technique. By benchmarking advanced object detection models across both CT and GPR datasets, this study evaluates the feasibility of transferring laboratory-validated fatigue crack detection to real-world pavement assessment. The overall research workflow and data integration strategy adopted in this study are summarized in the methodology flowchart presented in Fig. 1.

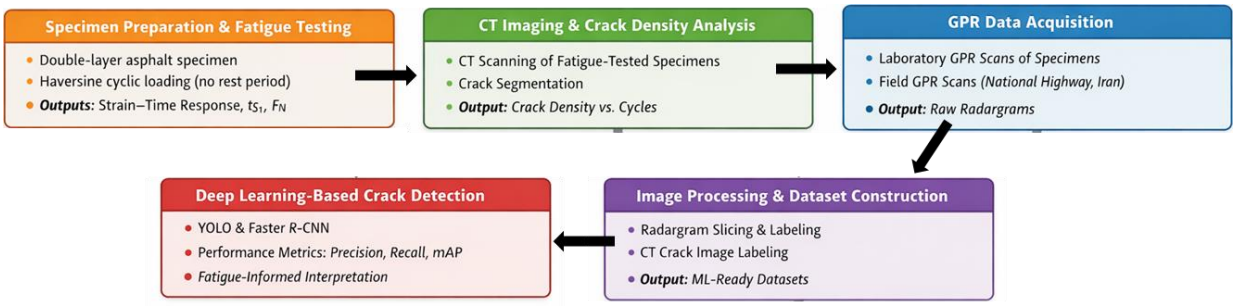

Fig. 1. Methodology flowchart of the proposed fatigue-informed multi-modal assessment framework

2. Materials and test methods

2.1. Raw materials

2.1.1. Bitumen

Neat bitumen with a penetration grade of 60/70, characterized in Table 1, was used in this study to fabricate the asphalt mixture.

2.1.2. Aggregate

The siliceous aggregates used in this study were separated into fine and coarse fractions. The physical properties of each fraction were determined in accordance with relevant ASTM standards and are summarized in Table 2. The aggregate gradation curve is presented in Fig. 2. The upper and lower standard limits of ASTM D 2487-92 were considered for dense grading of the aggregates used in this study [31].

Table 1. Specifications of neat bitumen.

Property	Standard	Quantity	Acceptable Range
Specific gravity (-)	ASTM D-7	1.03	1.00 - 1.05
Penetration (0.1 mm) at 25°C	ASTM D5-73	65.2	60 - 70
Softening point (°C)	ASTM D36-76	48.8	45 - 55
Ductility (cm) at 25°C	ASTM D113-79	>100	≥ 100
Loss of heating (%)	ASTM D1754-78	0.74	≤ 1.0
Flash point (°C)	ASTM D92-78	312	≥ 230
Kinematic viscosity (mPa.s) @ 135°C	ASTM D4402	328.2	300 - 500

Table 2. Physical properties of fine and coarse aggregates

Property	Standard	Fine Aggregate	Coarse Aggregate
Bulk specific gravity	ASTM C127 / C128	2.60	2.65
Apparent specific gravity	ASTM C127 / C128	2.68	2.72
Water absorption (%)	ASTM C127 / C128	1.2	0.8
Los Angeles abrasion loss (%)	ASTM C131	–	22
Flat and elongated particles (%)	ASTM D4791	–	8
Sand equivalent (%)	ASTM D2419	78	–
Fines content passing No. 200 (%)	ASTM C117	3.5	1.2

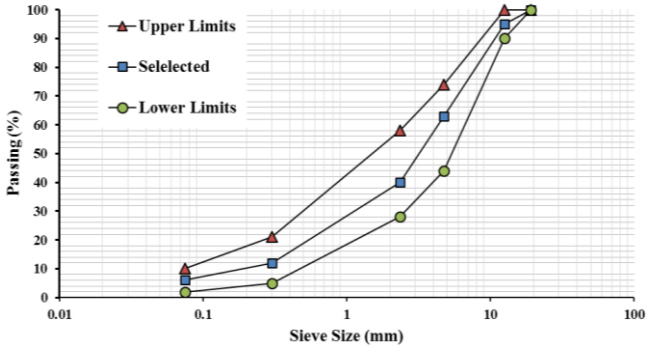

Fig. 2. Gradation curve of siliceous aggregate used in this study

2.2. Sample preparation

The optimum bitumen content (OBC) of the asphalt mixture was determined according to the Marshall Mix design, i.e., ASTM D1559. The OBC was equal to 5.8% for heavy traffic loading conditions. This mix design was applied to fabricate the asphalt mixture slabs with a target air void of 4% using a PReSBOX device, as shown in Fig. 3a. Then, the slab was cut into two layers. Both of these layers were used as the lower layer of a pavement, which represent the base or old pavement [32]. In order to simulate a reflective crack, under cyclic loading, existing in the old pavement layer, a notch with a depth of 20 mm and a thickness of 5 mm was created in the lower layer (Fig. 3b). This notch was covered with a temporary filler to protect it from being filled with new asphalt materials [33]. After preparation of the lower asphalt layer and creation of the artificial notch, the specimen was allowed to cool completely to room temperature. This cooling step ensured stabilization of the air void structure of the lower layer prior to the placement of the upper asphalt mixture. Subsequently, the required amount of new asphalt mixture was placed on top of the cooled lower layer and compacted using the PReSBOX device to achieve the target thickness, dimensions, and density of the upper layer. In other words, this amount of new asphalt mixture was added on the top of the previous layer (with a thickness of 70 mm) into the PReSBOX device to compact the materials and reach the desired density and dimensions of the upper layer (with a thickness of 50 mm). It should be noted that, similar to field practice, a tack coat consisting of a cationic slow-setting bitumen emulsion (CSS-1) with an application rate of 0.5 kg/m² was applied to ensure adequate bonding between the lower and upper asphalt layers [34-35]. After the completion of the compaction and cooling process of the upper layer, the temporary filler was ejected from the notch. As a result, a double-layer system with a notch, as shown in Fig. 3c, was prepared to perform the fatigue-loading test. It should be noted that this approach of sample preparation was selected based on the previous related studies [36–39].

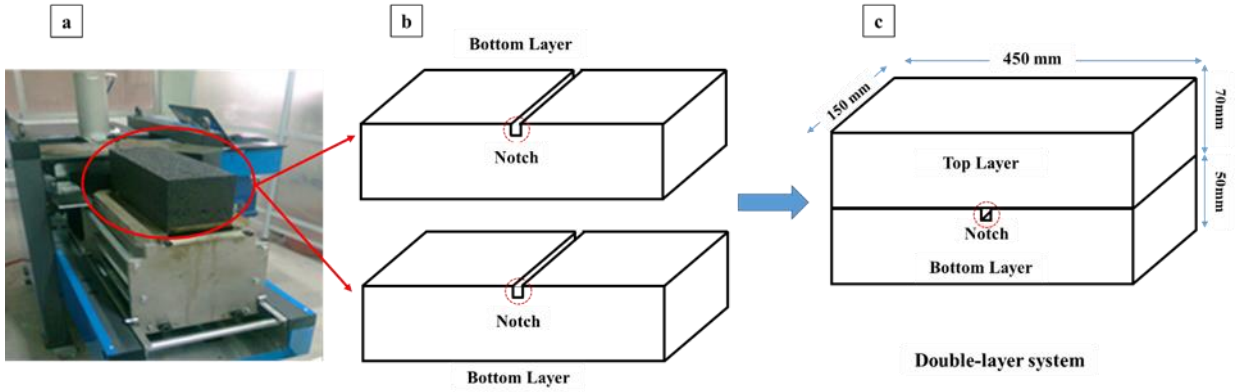

Fig. 3. a) Fabrication the mixture slabs using the PReSBOX device, b) Creating the notch in lower layer, and c) Final double-layer system of asphalt mixture

2.3. Fatigue test

A haversine cyclic loading under stress control mode was applied on a steel circle plate located on the top surface of the slab mixture to observe the fatigue cracking. To this aim, a maximum load of 6.9 kN, which is equal to a pressure of 690 kN/m2 (100 psi), was used to perform the fatigue test.

In addition, to keep contact between the landing actuator and mixture slab, a minimum load of 0.1 kN was applied in each loading cycle. A constant frequency of 10 Hz was applied to conduct the traffic at high speed. This haversine loading protocol without an imposed rest period was intentionally adopted to suppress viscoelastic recovery/healing effects and to promote progressive damage accumulation. This approach facilitates clearer identification of fatigue damage stages (e.g., tst and FN) and supports consistent correlation between mechanically defined fatigue progression and imaging-based crack evolution. Similar continuous haversine-type loading has been reported in prior studies on multi-layer asphalt overlay/reflective cracking systems and in fatigue investigations focusing on damage evolution rather than healing-dominated endurance testing [40–43]. Moreover, to simulate the real conditions, a neoprene rubber mat with an elastic modulus of 11000 MPa was placed under the mixture slab to represent the subgrade in the field. An intermediate temperature of 20°C was selected to perform the fatigue test. The outer surface of the upper layer was painted white to create a contrast between the crack and slab surface, allowing the crack propagation detection more clearly. Fig. 4 illustrates the fatigue loading apparatus and specimen setup used during laboratory testing. The fatigue test was continued until the crack reached the top of the overlay and the plastic horizontal strain occurred in the specimen.

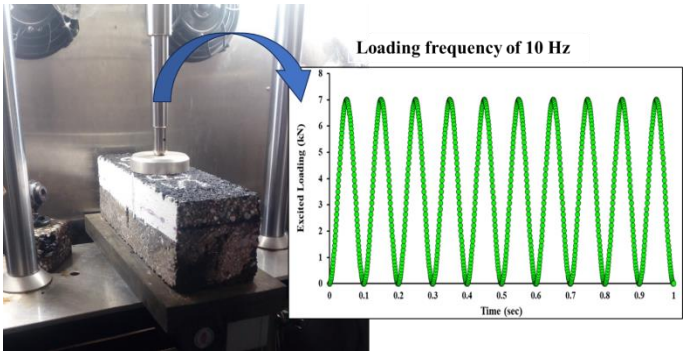

Fig. 4. Laboratory fatigue loading setup for the double-layer asphalt specimen at frequency of 10 Hz

Fig. 3 illustrates the actual laboratory specimen preparation procedure, including the fabricated asphalt slabs, the artificial notch simulating reflective cracking, and the final double-layer configuration. Fig. 4 shows the experimental fatigue loading setup, including the loading plate, loading waveform, and test environment used to induce fatigue cracking under controlled laboratory conditions.

3. Data acquisition

In this study, three interdependent data streams are employed, each serving a distinct role within the proposed framework. Fatigue loading data provides a mechanically meaningful fatigue stages identified using a piecewise strain model. CT scan images are used to quantify internal crack evolution through the crack density (CD) index. GPR images represent a field-deployable non-destructive testing modality. Labeled CT and GPR images serve as inputs to deep learning models, while detected crack locations and performance metrics constitute the model outputs.

3.1. CT image acquisition

To capture detailed images with high resolution, the X-ray source and detector system of the CT scanner were carefully calibrated. Scanners acquired cross-section images of the asphalt specimen, and each image was taken at a regular interval of 0.11 mm so that the entire specimen volume was covered. Images were scanned as grayscale maps with 256 bits, allowing for a wide range of voxel intensity values. CT scan images provided detailed information regarding the internal structure and void distribution within the asphalt specimen. The use of this state-of-the-art CT scan device facilitates a comprehensive investigation into the internal features and heterogeneity underlying the asphalt slab sample. CT scanning was conducted on asphalt specimens after fatigue loading to capture internal crack initiation and propagation. Raw CT slices served as the primary data source for crack segmentation, crack density calculation, and subsequent deep learning-based crack detection.

3.1.2. CT data construction

Initially, the CT scan produced a volumetric representation of the asphalt specimen with voxels with varying grayscale values. Image enhancement techniques were applied to enhance image clarity and remove irrelevant details. CT slices were processed with median filters and grayscale transformations [29]. In addition to improving visibility, these processes facilitated further analysis. The Roboflow software was used to detect and mark rectangular bounding boxes on the preprocessed images in preparation for YOLO and Faster RCNN. During this process, square images with a specific aspect ratio were scaled to ensure an approximate uniform height and width across the images. A labeled dataset of 1050 sample images with 5100 concealed crack annotations were then generated using augmentation techniques. A labeled dataset was divided into three subsets

by random selection: a training set (916 images), a validation set (89 images), and a test set (45 images) used to assess the model. In the following stages, various image processing algorithms and techniques will be applied to the preprocessed data. Using advanced image processing programs and machine learning algorithms, the specimen's characteristics can be thoroughly examined, allowing CT data to be correlated with its mechanical properties under fatigue loading, and GPR data to provide valuable insight. The multi-modal analysis will facilitate a better understanding of asphalt behavior and lead to more effective assessment and maintenance strategies.

3.2. GPR image acquisition

Images were acquired with a commercial GPR system equipped with a ground-coupled antenna operating at 2.3 GHz. The field GPR data were collected from an in-service flexible pavement section of a national highway in Iran. The surveyed section consisted of an asphalt surface layer over granular base and subbase layers. The purpose of the field survey was to evaluate the capability of GPR combined with deep learning models to detect concealed cracking patterns under real traffic conditions. These field data were used exclusively for training and evaluating the object detection models and were not involved in the mechanical fatigue calibration process. For both laboratory specimens, after loading and field tests carried out in a national highway of Iran, radar data were collected at 2 mm sampling intervals parallel to the radar line. An antenna was accurately positioned along a radar line using a survey wheel. This system used a time window of 10 ns and a high sampling frequency of 20 GHz (10 times the center frequency). Data captured by this setup allowed for fine details to be captured. For the comprehensive recording of distresses, all anomalies were observed from two different directions and from different origins for the asphalt specimen. Through this approach, the internal structure and any subsurface cracks in the asphalt specimen could be assessed comprehensively. In addition to the CT scan data, GPR images will contribute to a better understanding of asphalt's structural properties and defects. Due to space limitations, representative GPR radargrams are not exhaustively presented; however, labeled examples used for model training and evaluation are provided to illustrate typical fatigue-related crack signatures. Both laboratory-scale GPR measurements on fatigue-tested specimens and field-scale GPR surveys on an in-service highway were conducted. Raw radargrams obtained from these measurements were processed, segmented, and labeled to generate the image datasets used for deep learning-based crack detection. GPR-based crack detection is interpreted in this study within the fatigue-informed framework established through laboratory testing and CT validation, rather than as an independent anomaly detection task.

3.2.1 GPR data construction

GPR image creation consists of three steps: data processing, resizing, and labeling. Each of the mentioned items will be explained as follow:

3.2.1.1. Radar data pre-processing

Once the GPR images are acquired, it is crucial that appropriate filters are applied to improve the data quality. To mitigate the effects of wave propagation on all radar images obtained during test measurements, a subtractive mean dewow filter was utilized. Moreover, a background removal filter was used to remove anomalies, caused by wave propagation that affected the entire data set, performed in the same way as related articles [12]. Further, it was determined that the wave velocity for the GPR at 2.3 GHz was 0.1 m/ns.

3.2.1.2. Resizing

To comply with the requirements of the YOLO model, the captured GPR images were resized in multiples of 32 pixels. Images of 320 pixels by 320 pixels were derived from the GPR data. Considering that the actual size of the GPR images for the asphalt field sample was 0.18m x 120m, these images were divided into smaller segments with a consistent depth and length of 0.18m x 2m. Considering that the road structure's length is significantly greater than its depth, the length-to-width ratio of the captured images has been carefully calculated.

3.2.1.3. Labeling

Manually labeling concealed cracks in recorded GPR images was accomplished using Roboflow software. Subsurface cracks were identified by annotating rectangular boxes around them. Using two points along its diagonal, each box's coordinates were computed, capturing the crack's location and size. In the second step, the same software generated additional images for model training using data augmentation techniques. A total of 395 images were labeled and randomly separated into three groups for training, validation, and evaluation of the model. Among the 317 images included in the training set were 51 images in the validation set, and 17 images in the test set. The labeled GPR images represent processed forms of raw radargrams acquired during laboratory and field measurements. These images constitute the direct inputs to the YOLO and Faster R-CNN models used in this study.

4. Object detection algorithms

Nowadays, the use of computer vision has caused a huge change in various fields. Deep learning and computer vision have helped a lot in image analysis and classification. Image analysis with the help of deep learning falls into three main categories: Image classification, object detection and

segmentation are the three main approaches to analyze images. In the classification, the algorithm classifies each image into predefined classes. In these algorithms, the most important purpose is to determine the presence or absence of the objects. In addition to classification, object detection algorithms determine the desired objects' locations. In the segmentation method, in addition to recognizing the category and location of the object, the photo is separated from the background [44].

Among pavement image analysis algorithms, object detection is particularly popular. The ability of these algorithms to detect and localize pavement distresses is an important reason for this popularity. These algorithms are classified into two main categories (1) one-stage detectors and (2) two-stage detectors. In two-stage detectors, classification and localization are performed in two separate steps while in one-stage detectors, while both classification and localization are performed all at once. This method speeds up the algorithm compared to two-stage object detection algorithms. In this study, both one-stage and two-stage object detection algorithms were applied and the results were compared. Hyperparameter tuning was conducted using a grid-based empirical approach. Key hyperparameters, including learning rate, batch size, number of training epochs, and detection confidence threshold, were systematically varied, and the optimal configuration was selected based on performance on a validation dataset.

4.1. YOLO architecture

YOLO is one of the most common one-stage object detection algorithms. Generally, in this algorithm, the input image is divided into S×S grid. At the same time, bounding boxes and confidence scores are predicted by each grid cell [45]. This will help the algorithm to figure out which box is more likely to contain an object. Fig. 5 illustrates this method.

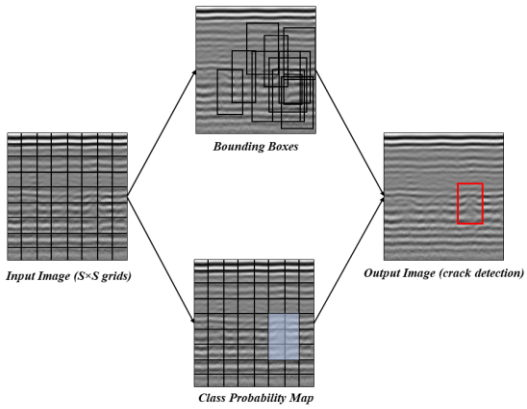

Fig. 5. The Detection Method of the YOLO Models

Generally, as shown in Fig. 5, modern YOLO models such as YOLOv3, YOLOv5, and YOLOv7 consist of three main components: (1) Backbone, (2) Neck, and (3) Head. In the backbone, the features are extracted from the input image using convolutional layers and these feature maps are collected, combined, and sent to the head by the neck. Finally, fully connected layers in the head will predict the outputs, which are the coordinates of bounding boxes and the predicted classes. The architectures of YOLO models are very similar to each other. In the YOLOv3, the backbone is Darknet53 which consists of a Convolutional layer (including convolution filter, batch normalization, and activation function which is usually Leaky-ReLU) and residual units. The neck uses a Feature Pyramid Network (FPN) and at the end, the YOLO layer plays the role of the head to predict the outputs. A similar architecture is used for YOLOv5 with the difference that instead of Darknet53, Cross-Stage Partial Net based on Darknet53 (CSPDarknet53) was used for the backbone with sigmoid activation function, and instead of FPN in the neck, Path Aggregation Network (PANet) was used. In addition to these layers, YOLOv5 uses a Spatial Pyramid Pooling (SPP) as a pooling layer [46]. In the YOLOv7, the backbone consists of Extended Efficient Layer Aggregation Network (E-ELAN) to enhance the learning process. Furthermore, model scaling is performed to make the model more accurate and faster. In the YOLOv7, a compound model scaling is used. In YOLOv7 models, the Re-parameterized techniques and auxiliary heads are used to improve the results. In general, relative to previous versions, YOLOv8 accuracy and speed has been enhanced. This model employed multiple backbones such as ResNet and CSPDarknet and its head consists of convolutional layers followed by fully connected layers. In this study, an attempt has been made to evaluate the performance of different models that include older and newer versions of them.

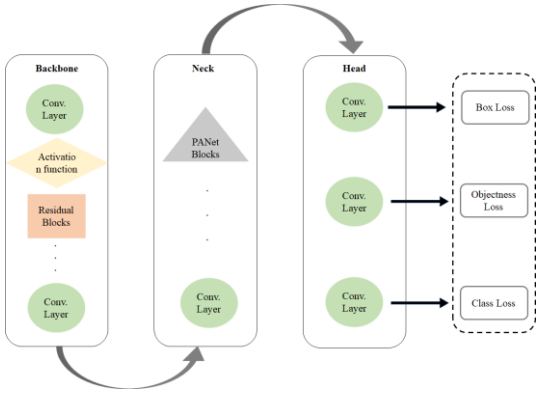

Fig. 6. Network Architecture of YOLO.

4.2. Faster-RCNN architecture

One of the most popular two-stage object detection algorithms is Faster-RCNN. This model is composed of two parts. The first module is called Regional Proposal Network (RPN), which is a deep fully convolutional network, and its task is to propose regions. The second part is a Fast R-CNN detector, and one of the most important components of Faster R-CNN is the backbone [47]. Different types of

backbones are used in Faster R-CNN such as Resnet50, Squeezenet, VGG, Mobilenet, and Darknet. Features are extracted by the backbone of the algorithm and the RPN uses the generated feature maps to propose bounding boxes with objectness scores. In the final step, ROI pooling layer uses the proposed bounding boxes and feature maps as inputs and the final outputs, which are predicted classes, and locations are obtained [48].

4.3. Experiment setup

A comparison of six one-stage and three two-stage object detection models was conducted to detect fatigue cracks in CT and GPR images, as shown in Table 3.

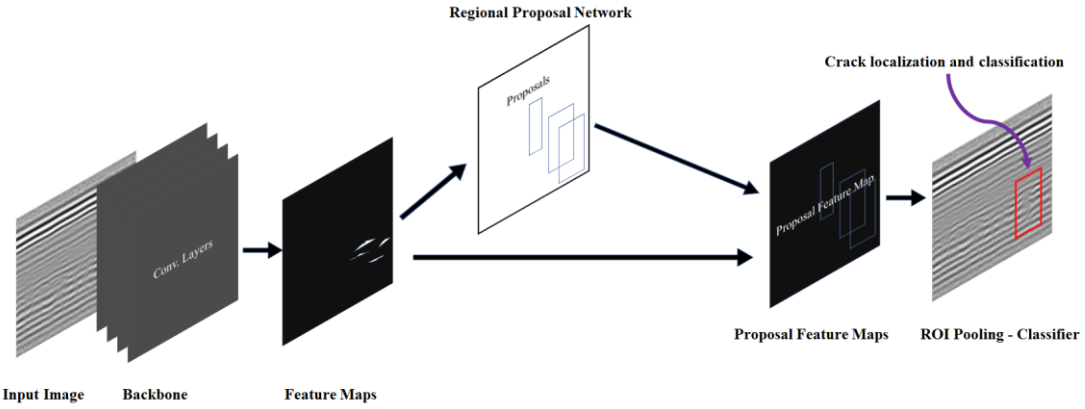

Fig. 7. Network Architecture of Faster-RCNN.

Table 3. Number of parameters for each model.

Type	Standard	Quantity
One-stage models	YOLOv3	61,529,119
	YOLOv3tiny	8,861,918
	YOLOv5s	7,022,326
	YOLOv5m	20,871,318
	YOLOv5l	46,138,294
	YOLOv5x	86,224,543
	YOLOv7	37,201,950
	YOLOv8	3,157,200
Two-stage model	Faster R-CNN Resnet50	41,299,161
	Faster R-CNN Mobilenetv3_large	18,930,229
	Faster R-CNN Squeezenet1_1	29,871,765

The models were trained, validated, and tested on a Google Colab server using 11.6 CUDA on a Tesla V4 GPU with 16 GB of RAM. With the PyTorch library version 1.13.1 as the experimental framework, the main algorithm was coded in Python. Cross-validation results were used to select hyperparameters for the models, as indicated in Table 4. A fair comparison was attempted by choosing similar hyperparameters for both YOLO and Faster R-CNN models.

Table 4. Chosen hyper-parameters.

Hyper-parameters	YOLO	Faster R-CNN
Batch size	16	16
Epochs	100	100
Learning rate	0.01	0.01
Momentum	0.0005	0.0005
Weight decay	0.937	0.9
Input image size	640×640	640×640

In the training process, overfitting was possible due to the limited number of images compared to model parameters. The transfer learning technique was employed in order to address this concern. Transfer learning is a widely used method in deep learning-based models, especially for detecting pavement distress [49]. By leveraging pre-trained weights from a large dataset, it initializes the network's parameters before fine-tuning them on a smaller dataset. Particularly in scenarios with limited labeled data, this strategy significantly improves the model's performance. Using the pre-trained COCO dataset, transfer learning was used to initialize the model's weights. COCO contains over 200,000 labeled images and consists of 80 classes of objects, making it an ideal resource for pre-training object detection algorithms. A model based on transfer learning was designed to classify surface cracks and concealed cracks in CT-scan images for the specific task of detecting cracks. Through the use of transfer learning, this experiment aimed to increase the performance and accuracy of the models in detecting fatigue cracks based on CT and GPR images available in this study by leveraging knowledge gained from a diverse and extensive dataset like COCO.

4.4. Model evaluation metrics

To evaluate the performance of the model, different quantitative metrics are utilized. One of the most important criteria is intersection over Union (IOU). This metric compares the predicted bounding boxes obtained from the model to the ground truth bounding boxes [45,50]. Eq. (1) illustrates the IOU mathematically.

$$\mathbf{IOU} = \frac{|\boldsymbol{B_p} \cap \boldsymbol{B_{gt}}|}{|\boldsymbol{B_p} \cup \boldsymbol{B_{gt}}|} \quad (1)$$

In Eq. (1), B_p is the predicted bounding box, and B_g is the ground truth bounding box [51, 52]. The numerator of this deduction is the union of the predicted and ground truth boxes area, and the denominator of the deduction is the intersection of boxes. This deduction demonstrates the proficiency in predicting and fitting the bounding boxes [4]. In this study, the IOU threshold was chosen as 0.5. In other words, when more than 50 percent overlap between predicted and ground truth bounding boxes was observed, the existence of the object in the predicted bounding box will be confirmed, and it means that the object is correctly detected so it indicates a true positive (TP). If the model predicts that there are distresses in an image incorrectly, it is a false positive (FP). If the model incorrectly predicts no distresses, it is a false negative (FN). Finally, if the model predicts that there is no distress correctly, it is a true negative (TN). According to these parameters, some other important metrics are defined. Precision, recall, and F1 score are other essential metrics that are used repeatedly in machine learning and deep learning. Eqs. (2) to (4) present these metrics.

$$\text{Precision} = \frac{TP}{TP + FP} \tag{2}$$

$$\text{Recall} = \frac{TP}{TP + FN} \tag{3}$$

$$\text{F1-score} = 2 \times \left(\frac{Precision \times Recall}{Precision + Recall}\right) \tag{4}$$

The precision presents the accuracy of the model and the recall implies the ability of the model to predict properly. The F1-score is a combined index that expresses the overall performance of the model.

By drawing the Precision-Recall curve (P-R curve) and calculating the area under it, another important metric will be obtained which is called average precision (AP). In the other word, AP summarizes the P-R curve into a single value. By calculating the mean of the AP values, the mean average precision (mAP) will be obtained. These metrics investigate the overall performance of the model [19].

5. Result

5.1. Fatigue results

The horizontal strain curves for different slab mixtures were analyzed using Zhou et al.'s model [53], represented by Eqs. (5) to (7). There are three domains in this piecewise function: a power-law function (Eq. (5)), a linear function (Eq. (6)), and an exponential function (Eq. (7)):

$$\text{if } t \le t_{ps};\ \varepsilon_p = a\, t^{b};\ \ \varepsilon_{ps} = a\, t_{ps}^{b} \tag{5}$$

$$\text{if } t_{ps} \le t \le t_{st};\ \ \varepsilon_p = \varepsilon_{ps} + c\,(t - t_{ps});\ \ \varepsilon st = \varepsilon ps + c\,(t_{st} - t_{ps}) \tag{6}$$

$$\text{if } t \ge t_{st};\ \ \varepsilon_p = \varepsilon_{st} + d\,[e^{f\,(t - t_{st})} - 1] \tag{7}$$

In Eqs. (5) to (7), t stands for loading time, and a, b, c, d, and f are constants determined by curve fitting. In the permanent strain curve, the time t_{ps} and t_{st} correspond to the initiation of the second stage (ε_{ps}) and third stage (ε_{st}), respectively. This flow number (FN) is equal to t_{st}, which represents the plastic flow of asphalt mixtures under cyclic loading [37]. Fatigue distress resistance increases with increasing FN. Fig. 8 illustrates the results of an experiment on accumulative horizontal stain under fatigue load as well as the predictions of the piecewise function.

Fig. 8 presents a representative accumulative horizontal strain–time response obtained from the fatigue tests. Similar strain evolution trends were observed for all tested specimens, with variations in fatigue life parameters depending on loading conditions. Fig. 8 illustrates the predicted results of the piecewise function, indicating the model is effective at estimating asphalt mixture fatigue behavior. To compare the experimental results with the predicted ones, the T-test was used, with a 95% confidence interval. A significance value of less than 0.05 was found in the statistical analysis, suggesting no significant differences between the groups in mean values. As a result, the piecewise function estimates the accumulative horizontal strain with repeated loading. Moreover, the model's fitting outputs of Eqs. (5) to (7) enable the determination of the specimen's fatigue life, i.e., FN, and the loading number for the second stage of fatigue life, i.e., t_{st}. These cycle numbers, i.e., t_{st} and FN, denotes the initiation of micro-cracks and macro-cracks, respectively. The fatigue life parameters extracted from the piecewise strain model, including the initiation of the secondary fatigue stage (t_{st}) and the flow number (FN), were determined for all tested specimens. These parameters represent the onset of micro-crack initiation and macro-crack propagation, respectively, and form the mechanical basis for correlating fatigue behavior with imaging-based crack evolution.

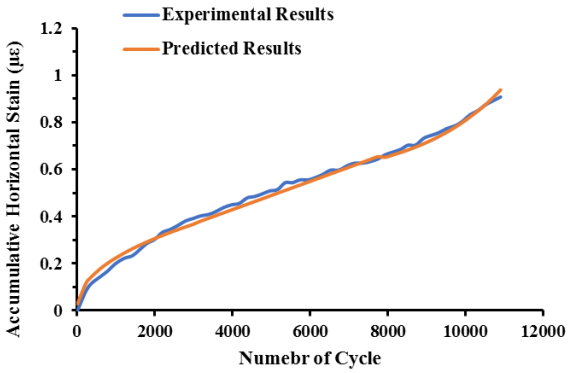

Fig. 8. Experimental and predicted results of accumulative horizontal stain under fatigue loading

In view of the fact that the corresponding cycles of the second and third fatigue stages were accurately determined by using piecewise functions, a threshold can be suggested to identify the initiation of these fatigue stages based on the

crack density (CD) index defined through image processing results generated from the CT scan technique. To achieve this, as shown in Fig. 9, a region was selected to calculate the CD index using Eq. (8):

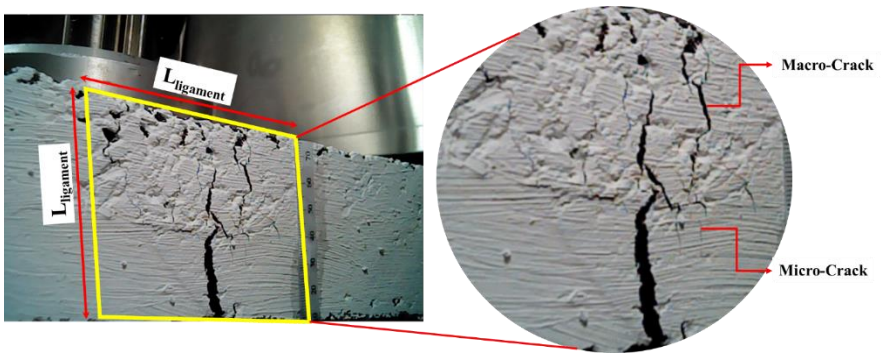

Fig. 9. Determining the crack-density in the specific area with the length and width of $L_{Ligament}$

$$\mathbf{CD} = \frac{\boldsymbol{A_{Crack}}}{\boldsymbol{A_{Ligament}}} = \frac{\boldsymbol{A_{Crack}}}{\boldsymbol{L_{Ligament}} \times \boldsymbol{L_{Ligament}}} \quad (8)$$

Where A_{Crack} denotes the total area of cracks in the sample, $A_{Ligament}$ is the specific area considered for the calculation of, A_{Crack} and $L_{Ligament}$ is the ligament length calculated by subtracting the specimen's height and the length of the initial notch. The crack density (CD) index provides a quantitative imaging-based damage metric that enables direct linkage between internal crack evolution observed in CT images and mechanically defined fatigue stages, including micro-crack initiation (t_{st}) and macro-crack initiation (FN). The crack images shown in Fig. 9 represent raw experimental observations obtained directly from laboratory fatigue-tested specimens. Both surface-visible and internally propagated cracks were captured and processed to quantify crack density.

A total of eight PDCNNs, including AlexNet, GoogleNet, SqueezNet, ResNet-18, ResNet-50, ResNet-101, DenseNet-201, and Inception-v3, were retrained using pavement images and transfer learning techniques to identify two types of pavement cracks: surface and concealed cracks, as shown in Fig. 10.

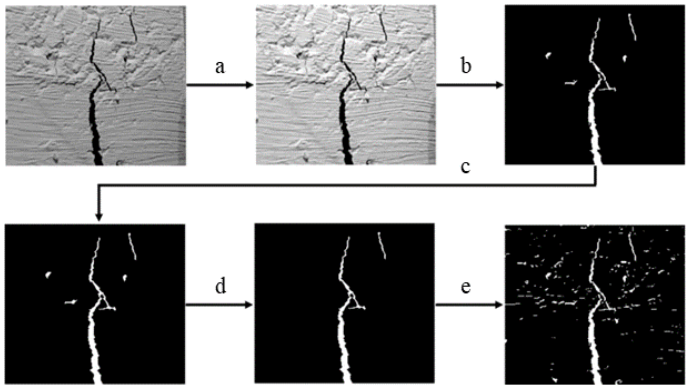

Fig. 10. Crack segmentation process. a) Histogram equalization, b) Image smoothing, c) Wavelet transform, d) Thresholding, and e) Morphological filtering

The calculated crack density was obtained for both t_{st} and FN cycles, and their relationship with CD is shown in Figs. 11a and 11b, respectively. Six samples were tested under various loading conditions, resulting in varying fatigue lives.

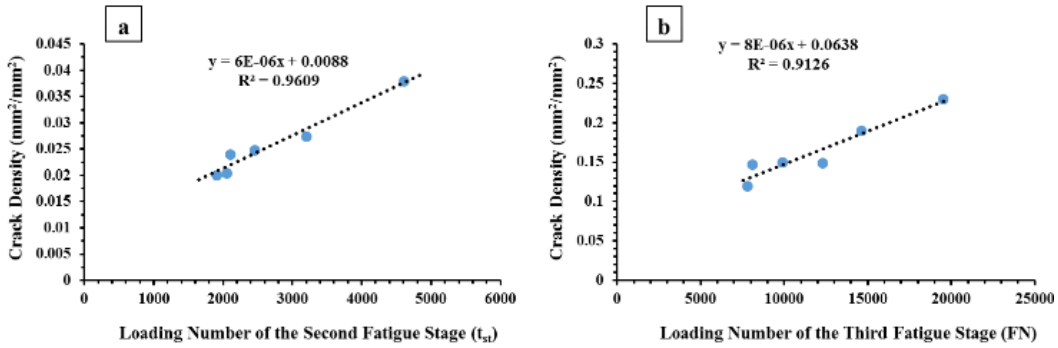

Fig. 11. The relationship between CD and a) t_{st} and b) FN for different fatigue lives

It is significant to note that the crack density was not only calculated for the external visible surface of the sample but also for the internal surfaces, which are invisible using CT images. For this purpose, four internal longitudinal surfaces within the specimen were considered, located at 30 mm intervals from one another (Fig. 11a). By using CT image processing, crack density was determined for each internal surface. Similar to Figs. 11a and 11b, the crack density values of the internal surfaces corresponding to t_{st} and FN are presented in Figs. 12b and 12c, respectively.

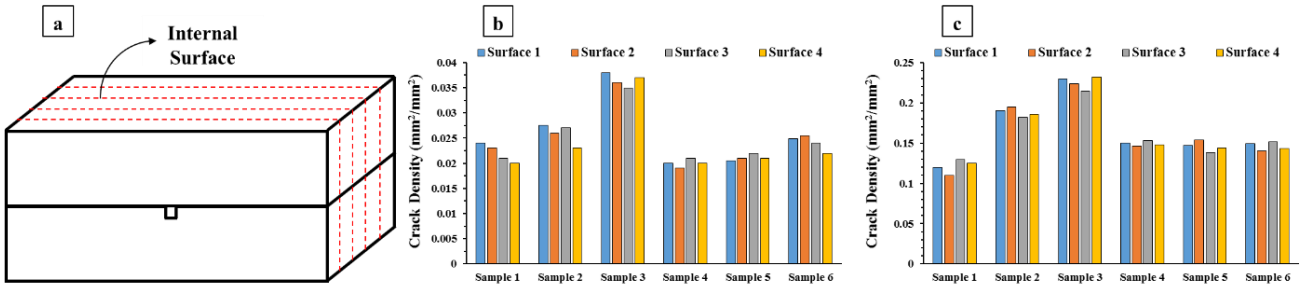

Fig. 12. a) Considering four internal longitudinal surfaces within specimen, b) the relationship between CD and t_{st} and c) the relationship between CD and FN for different fatigue lives

According to Figs. 12a and 12b, CD strongly correlates with the number of loadings applied to the sample at both the beginning and end of its life. In addition, Fig. 12 shows that the CD values calculated for the internal surfaces of the asphalt mixture are the same as those calculated for the external surfaces. As a result, the CT scan technique can effectively estimate fatigue cracking in asphalt mixture zones, even those that are invisible. Further, Figs. 12a and 12b demonstrate that the CD value and relationships in these figures can be used to determine the initiation stage of micro-cracks and macro-cracks. In this manner, a reliable estimate of the initiation of the second or third fatigue stage of the pavement can be obtained by using CT scan images taken at different depths of the pavement and determining their CD values. As a result of this knowledge, it becomes easier to implement appropriate actions for repair and maintenance operations, effectively estimating the remaining pavement life. The observed relationships between crack density (CD) and fatigue life parameters (t_{st} and FN) demonstrate that CT-derived imaging metrics provide a quantitative interpretation of fatigue damage evolution, enabling identification of fatigue stages through internal crack development. The increase in crack density with progressing fatigue cycles reflects the transition from micro-crack initiation to macro-crack propagation, demonstrating that CT-derived CD evolves consistently with mechanically defined fatigue stages.

5.2. Model training results

5.2.1. YOLO

The mean Average Precision (mAP) of YOLO models was used to compare the performance. Various YOLO models' Precision-Recall (P-R) curves are shown in Fig. 13. This chart reflects the precision and recall capabilities of the models by the area under the curve (AUC).

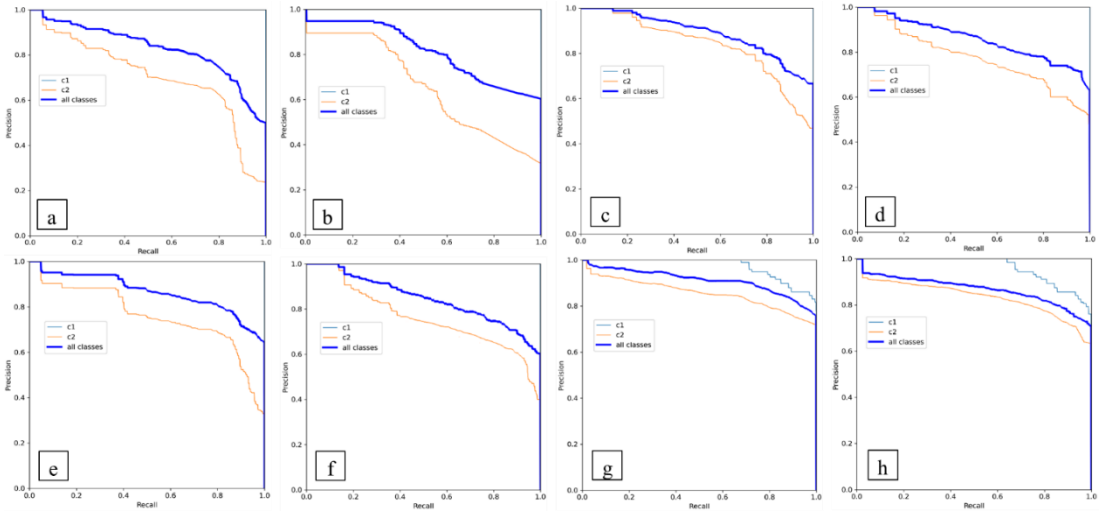

Fig. 13. Precision and recall of the Various YOLO models

Fig. 13 shows that the C1 curve, representing larger cracks, has a larger area than the C2 curve, showing that all models are better at detecting large cracks than small cracks. However, the models performed acceptably when classifying small cracks (C2). Fig. 14 presents the P-R curves for GPR images for a single crack class.

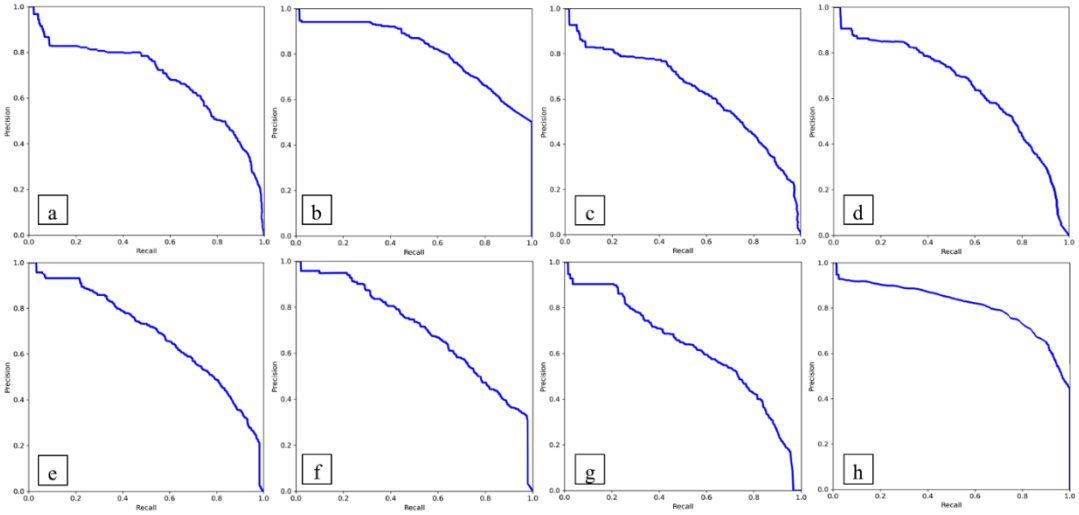

Fig. 14. Precision and recall of the Various YOLO models for GPR images.

In Table 5, CT dataset mAP values were approximately 10-20% higher than GPR dataset mAP values. Due to the larger number of images in the CT dataset compared to the GPR dataset, the greater number of images may mitigate overfitting issues. Overfitting becomes a concern when model parameters outnumber images, and the accuracy of the model improves as the number of images increases.

Table 5. Training Results of Eight Models.

Model	GPR				CT			
	Precision (%)	Recall (%)	F1-score (%)	mAP (%)	Precision (%)	Recall (%)	F1-score (%)	mAP (%)
YOLOv3	73.6	75.7	74.6	70.7	90.4	90.1	90.2	88.0
YOLOv3-tiny	72.9	67.7	70.2	68.1	85.5	86	85.7	86.2
YOLOv5s	73.5	78.6	75.9	77.1	91.6	88.3	89.9	91.6
YOLOv5m	72.6	80.8	76.4	75.7	92.1	87.5	89.2	89.9
YOLOv5l	74.4	76.2	75.3	74.6	90.8	86.6	88.6	88.7
YOLOv5x	75.8	76.1	75.9	76.8	90.5	89.6	90.0	89.1
YOLOv7	72.0	86.6	78.4	78.6	71.4	78.3	74.6	73.0
YOLOv8	74.4	79.5	76.8	75.6	89.5	85.8	87.6	89.2

The YOLOv7, YOLOv5s, and YOLOv8 models outperformed other models on the GPR dataset, while the YOLOv5s, YOLOv5m, and YOLOv8 models outperformed others on the CT dataset. Based on these results, it appears that smaller and medium YOLO models, as well as the latest versions (YOLOv8 and YOLOv7), are more accurate at detecting pavement concealed cracks, gathered by GPR and CT scan techniques.

5.2.2. Faster R-CNN

On both CT and GPR datasets, Faster R-CNN models displayed inferior performance compared to YOLO models except for YOLOv3 and YOLOv3-tiny, which had lower mAP values. Moreover, the Faster R-CNN models took significantly longer to train and execute than the YOLO models. YOLO models are one-stage object detection models that bypass region proposal, thus resulting in this disparity in speed. Additionally, YOLO models performed better on datasets with small objects than Faster R-CNN models. As a result, Faster R-CNN models performed better on the GPR dataset with a single class, while YOLO models performed better on the CT dataset with two classes representing small and large cracks. This difference in performance can be attributed to the abundance of data in the CT dataset. The metrics for the Faster R-CNN models are shown in Table 6.

Table 6. Training Results of Eight Models.

Model	GPR				CT			
	Precision (%)	Recall (%)	F1-score (%)	mAP (%)	Precision (%)	Recall (%)	F1-score (%)	mAP (%)
Faster R-CNN ResNet50	71.98	74.81	73.37	72.3	74.44	72.66	73.54	71.6
Faster R-CNN MobileNetV3-Large	68.16	70.03	69.08	68.7	63.53	68.42	65.88	66.2
Faster R-CNN SqueezeNet1-1	63.24	64.77	64.00	63.0	51.49	53.11	52.29	50.9

As summarized in Tables 4 and 5, YOLO models achieved higher mAP than the three Faster R-CNN backbones on both datasets. On GPR images, the best YOLO models (YOLOv7 and YOLOv5s) exceeded the best Faster R-CNN (ResNet50). On CT images, the gap was substantially larger, where YOLOv5s/YOLOv5m/YOLOv8 reached ~89–92% mAP compared with 51–72% mAP for Faster R-CNN. This indicates that one-stage detectors generalize better in the CT two-class setting and small-object crack patterns under the available training data.

The loss values-epochs curve for the discussed models is shown in Fig. 15. In the course of training, the loss function decreases until it converges to a nearly constant value. The goal is to determine the optimal number of epochs for training. YOLO models performed better than Faster R-CNN models in detecting cracks in GPR and CT datasets, while Faster R-CNN models were less accurate and less efficient in training. Using GPR and CT images, these results confirm the effectiveness of YOLO models, particularly the smaller versions (YOLOv5s and YOLOv5m).

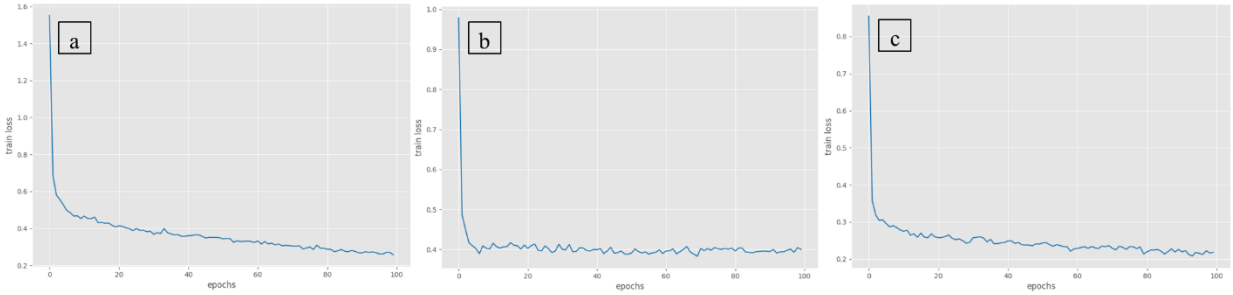

Fig. 15. The results of a) Resnet-CT, b) Mobilenet-CT, c) Squeezenet-ct.

6. Discussion

In this study, the piecewise function model of Zhou et al. [53] was successfully applied to study fatigue behavior in different asphalt slab mixtures. Through T-test analysis, the model accurately predicted accumulative horizontal strain during fatigue loading with no significant difference between experimental and predicted results. The knowledge of fatigue life and crack initiation (t_{st} and FN) can improve the determination of pavement fatigue resistance and provide a reliable prediction of the remaining life of pavement for timely maintenance. It should be emphasized that the role of deep learning in this study is not to directly predict fatigue life, but to automate the detection of fatigue-related cracking patterns in imaging data. By validating crack density evolution against fatigue stages using CT scans, deep learning-based crack detection enables fatigue-informed interpretation of GPR data, which is essential for scalable field-level pavement assessment. Further, deep learning algorithms were used to detect pavement concealed cracks from CT scan images. Using transfer learning, eight pre-trained deep convolutional neural networks (PDCNNs) were retrained for accurate crack detection and classification. A comparison of YOLO and Faster R-CNN models showed that YOLO models performed better on both GPR and CT datasets in terms of mean average precision (mAP). On the GPR dataset, YOLOv7, YOLOv5s, and YOLOv8 excelled, whereas on the CT dataset, YOLOv5s, YOLOv5m, and YOLOv8 outperformed others.

CT scanning provides a high-resolution reference for internal fatigue crack evolution, enabling validation of crack patterns detected using GPR. The consistency between CT-derived crack density trends and GPR-based crack detection confirms that GPR observations capture fatigue-related damage mechanisms rather than isolated anomalies. In diverse and complex datasets like CT images, YOLO's one-stage object detection approach and better performance with small objects contributed to its efficiency. Unlike other related studies, this research combines fatigue tests, imaging, and deep learning. By linking fatigue stages identified through mechanical testing (t_{st} and FN) with CT-derived crack density evolution, this study establishes a

physically meaningful basis for interpreting imaging-based crack detection results. Consequently, deep learning-based crack detection in CT and GPR images reflects fatigue-driven damage progression rather than purely geometric crack features. Using CT scan data in conjunction with a piecewise function enhances the understanding of pavement fatigue. The application of transfer learning to crack detection illustrates the potential of AI-based techniques for assessing infrastructure conditions. Research in this area includes [19], using GPR and deep learning to detect concealed cracks in small datasets. A network-in-network model was discussed in [16] for detecting pavement distress. To achieve acceptable real-time detection accuracy, [17] used GPR and Faster R-ConvNet. [54] used CNNs for concealed crack recognition in asphalt pavement through GPR images. For segmenting small cracks in asphalt pavement, [18] used mask region-based RCNN. As mentioned previously, the research has mainly focused on detecting concealed cracks in pavements using GPR and machine learning. However, these results demonstrate the effectiveness of deep learning models in real-time crack detection, irrespective of concealed crack types, and comparing them with other NDT systems based on results and validation of GPR.

The results of this study indicated that fatigue cracks were found in the images obtained via GPR and CT scan of specimens and that concealed cracks were found in field data obtained by GPR. However, due to the small sample size of GPR data, it is beyond the scope of this study to classify fatigue cracks in field data. Deep learning-based crack detection does not operate independently of fatigue behavior; instead, it enables automated identification of crack features whose evolution has been physically linked to fatigue stages through mechanical testing and CT-derived crack density analysis. Therefore, the exploration and comparison of various YOLO and Faster R-CNN models, using techniques such as transfer learning, will enhance pavement crack detection research by recommending YOLOv5s and YOLOv8 respectively for GPR and CT datasets, providing future researchers with valuable insight.

7. Conclusion

This study used imaging techniques and deep learning algorithms to enhance pavement distress detection. Asphalt samples were subjected to cyclic loading during the fatigue test. For the assessment of the internal structure and concealed cracks, CT scans and GPR images and CT scans (as a comparative method) were used to collect specimens and field data. A comparison was conducted between two object detection algorithms for detecting fatigue cracks in both types of images, YOLO and Faster-RCNN. A variety of metrics were used to evaluate the performance of the models, which were trained using transfer learning with pre-trained weights from the COCO dataset. Study results provided valuable insights and contributions for pavement assessment, including:

- The fatigue behavior of different asphalt slab mixtures was properly assessed using Zhou et al.'s piecewise function model, precisely estimating accumulative horizontal strain during fatigue loading.
- A statistical analysis using the T-test verified the accuracy of the model, showing that there was no significant difference between experimental and predicted results.
- Piecewise function provides information about the specimen's fatigue life and the initiation of micro-cracks and macro-cracks, essential for understanding fatigue resistance and predicting remaining asphalt pavement life.
- By retraining pre-trained deep convolutional neural networks (PDCNNs) using transfer learning, surface and concealed cracks could be accurately classified, which greatly enhanced crack detection and classification.
- In comparison of YOLO and Faster R-CNN models, YOLO models showed superior performance in mean Average Precision (mAP) for both GPR and CT datasets.
- The best models on the GPR dataset were YOLOv7, YOLOv5s, and YOLOv8, while the best models on the CT dataset were YOLOv5s, YOLOv5m, and YOLOv8.

As a result, this research provides significant insight into asphalt pavement fatigue behavior, which will pave the way for further advancements in pavement distress detection and maintenance practices.

8. Future work

Future work should expand the dataset to include diverse pavement types, weather conditions, and road infrastructures, enhancing model generalizability and accuracy. Integration of multi-modal data, like GPR and CT scans, with other non-destructive testing methods, can offer a comprehensive view of pavement conditions, improving distress detection reliability.

Credit Author Statement

Shaghayegh Alipour: Conceptualization, Resources, Methodology, Visualization, Software, Writing - Original Draft. **Mojtaba Khodadadi:** Conceptualization, Data curation, Formal analysis, Investigation, Validation, Resources, Methodology, Visualization, Software, Writing - Original Draft, Writing - Review & Editing, Supervision

Mohammad Javad Amani: Software, Visualization, Writing - Original Draft. **Ali Khodaii:** Writing - Review & Editing, Supervision. **Saeid Hesami:** Writing - Review & Editing, Supervision.

Acknowledgements

This work is partially supported by the Iran National Science Foundation (INSF).

Declaration of interests

The authors declare that they have no known competing financial interests or personal relationships that could have appeared to influence the work reported in this paper.

References

[1] H. Liu, X. Yang, L. Jiang, S. Lv, T. Huang, Y. Yang, Fatigue-creep damage interaction model of asphalt mixture under the semi-sine cycle loading, Constr. Build. Mater. 251 (2020) 119070. https://doi.org/10.1016/j.conbuildmat.2020.119070.

[2] Z. Zhang, S. Shen, B. Shi, H. Wang, Characterization of the fatigue behavior of asphalt mixture under full support using a Wheel-tracking Device, Constr. Build. Mater. 277 (2021) 122326. https://doi.org/10.1016/j.conbuildmat.2021.122326.

[3] A. Mahpour, S. Alipour, M. Khodadadi, A. Khodaii, J. Absi, Leaching and mechanical performance of rubberized warm mix asphalt modified through the chemical treatment of hazardous waste materials, Constr. Build. Mater. 366 (2023) 130184. https://doi.org/10.1016/j.conbuildmat.2022.130184.

[4] H. Qin, D. Zhang, Y. Tang, Y. Wang, Automatic recognition of tunnel lining elements from GPR images using deep convolutional networks with data augmentation, Autom. Constr. 130 (2021) 103830. https://doi.org/10.1016/j.autcon.2021.103830.

[5] J. Zhang, C. Zhang, Y. Lu, T. Zheng, Z. Dong, Y. Tian, Y. Jia, In-situ recognition of moisture damage in bridge deck asphalt pavement with time-frequency features of GPR signal, Constr. Build. Mater. 244 (2020) 118295. https://doi.org/10.1016/j.conbuildmat.2020.118295.

[6] Z. Tong, J. Gao, D. Yuan, Advances of deep learning applications in ground-penetrating radar: A survey, Constr. Build. Mater. 258 (2020) 120371. https://doi.org/10.1016/j.conbuildmat.2020.120371.

[7] J. Zhang, X. Yang, W. Li, S. Zhang, Y. Jia, Automatic detection of moisture damages in asphalt pavements from GPR data with deep CNN and IRS method, Autom. Constr. 113 (2020) 103119. https://doi.org/10.1016/j.autcon.2020.103119.

[8] Z. Liu, W. Wu, X. Gu, S. Li, L. Wang, T. Zhang, Application of combining yolo models and 3d gpr images in road detection and maintenance, Remote Sens. (Basel). 13 (2021) 1–18. https://doi.org/10.3390/rs13061081.

[9] M.G. Zamani, M.R. Nikoo, F. Niknazar, G. Al-Rawas, M. Al-Wardy, A.H. Gandomi, A multi-model data fusion methodology for reservoir water quality based on machine learning algorithms and bayesian maximum entropy, J. Clean. Prod. 416 (2023) 137885.

[10] W. Lei, F. Hou, J. Xi, Q. Tan, M. Xu, X. Jiang, G. Liu, Q. Gu, Automatic hyperbola detection and fitting in GPR B-scan image, Autom. Constr. 106 (2019) 102839. https://doi.org/10.1016/j.autcon.2019.102839.

[11] M. Rasol, J.C. Pais, V. Pérez-Gracia, M. Solla, F.M. Fernandes, S. Fontul, D. Ayala-Cabrera, F. Schmidt, H. Assadollahi, GPR monitoring for road transport infrastructure: A systematic review and machine learning insights, Constr. Build. Mater. 324 (2022). https://doi.org/10.1016/j.conbuildmat.2022.126686.

[12] F.M. Fernandes, J.C. Pais, Laboratory observation of cracks in road pavements with GPR, Constr. Build. Mater. 154 (2017) 1130–1138. https://doi.org/10.1016/j.conbuildmat.2017.08.022.

[13] M.A. Rasol, V. Pérez-Gracia, M. Solla, J.C. Pais, F.M. Fernandes, C. Santos, An experimental and numerical approach to combine Ground Penetrating Radar and computational modeling for the identification of early cracking in cement concrete pavements, NDT and E International 115 (2020). https://doi.org/10.1016/j.ndteint.2020.102293.

[14] M. Solla, S. Lagüela, H. González-Jorge, P. Arias, Approach to identify cracking in asphalt pavement using GPR and infrared thermographic methods: Preliminary findings, NDT and E International 62 (2014) 55–65. https://doi.org/10.1016/j.ndteint.2013.11.006.

[15] Z. Tong, J. Gao, H. Zhang, Recognition, location, measurement, and 3D reconstruction of concealed cracks using convolutional neural networks, Constr. Build. Mater. 146 (2017) 775–787. https://doi.org/10.1016/j.conbuildmat.2017.04.097.

[16] Z. Tong, D. Yuan, J. Gao, Y. Wei, H. Dou, Pavement-distress detection using ground-penetrating radar and network in networks, Constr. Build. Mater. 233 (2020) 117352. https://doi.org/10.1016/j.conbuildmat.2019.117352.

[17] J. Gao, D. Yuan, Z. Tong, J. Yang, D. Yu, Autonomous pavement distress detection using ground penetrating radar and region-based deep learning, Measurement (Lond). 164 (2020). https://doi.org/10.1016/j.measurement.2020.108077.

[18] Z. Liu, J.K.W. Yeoh, X. Gu, Q. Dong, Y. Chen, W. Wu, L. Wang, D. Wang, Automatic pixel-level detection of vertical cracks in asphalt pavement based on GPR investigation and improved mask R-CNN, Autom. Constr. 146 (2023) 104689. https://doi.org/10.1016/j.autcon.2022.104689.

[19] S. Li, X. Gu, X. Xu, D. Xu, T. Zhang, Z. Liu, Q. Dong, Detection of concealed cracks from ground penetrating radar images based on deep learning algorithm, Constr. Build. Mater. 273 (2021) 121949. https://doi.org/10.1016/j.conbuildmat.2020.121949.

[20] Z. Liu, X. Gu, J. Chen, D. Wang, Y. Chen, L. Wang, Automatic recognition of pavement cracks from combined GPR B-scan and C-scan images using multiscale feature fusion deep neural networks, Autom. Constr. 146 (2023) 104698. https://doi.org/10.1016/j.autcon.2022.104698.

[21] A.T. Papagiannakis, A. Abbas, E. Masad, Micromechanical analysis of viscoelastic properties of asphalt concretes, Transp. Res. Rec. 1789 (2002) 113–120.

[22] S. Saadeh, L. Tashman, E. Masad, W. Mogawer, Spatial and directional distribution of aggregates in asphalt mixes, J. Test. Eval. 30 (2002) 483–491.

[23] L. Banta, K. Cheng, J. Zaniewski, Estimation of limestone particle mass from 2D images, Powder Technol. 132 (2003) 184–189.

[24] L. Wang, H.S. Paul, T. Harman, J. D'Angelo, Characterization of aggregates and asphalt concrete using X-Ray computerized tomography-A state of the art report (with discussion), Journal of the Association of Asphalt Paving Technologists 73 (2004).
[25] R. Khan, A.C. Collop, G.D. Airey, A.N. Khan, Asphalt damage characterization from cyclic test and X-ray computed tomography, Proceedings of the Institution of Civil Engineers: Transport 166 (2013) 203–213. https://doi.org/10.1680/tran.11.00045.
[26] L. Gao, F. Ni, H. Luo, S. Charmot, Characterization of air voids in cold in-place recycling mixtures using X-ray computed tomography, Constr. Build. Mater. 84 (2015) 429–436. https://doi.org/10.1016/j.conbuildmat.2015.03.081.
[27] J. Hu, P. Liu, D. Wang, M. Oeser, Y. Tan, Investigation on fatigue damage of asphalt mixture with different air-voids using microstructural analysis, Constr. Build. Mater. 125 (2016) 936–945. https://doi.org/10.1016/j.conbuildmat.2016.08.138.
[28] D. Braz, R.C. Barroso, R.T. Lopes, L.M.G. Motta, Crack detection in asphaltic mixtures by computed tomography, NDT and E International 44 (2011) 195–201. https://doi.org/10.1016/j.ndteint.2010.11.005.
[29] Q. Li, H. Yang, X. Ma, F. Ni, Evaluation of microstructure and damage evolution for asphalt pavements in an advanced repeated load permanent deformation test using X-ray computed tomography, Road Materials and Pavement Design 18 (2017) 1135–1158. https://doi.org/10.1080/14680629.2016.1207555.
[30] Y. Li, W. Jiang, J. Shan, P. Li, R. Lu, B. Lou, Characteristics of void distribution and aggregate degradation of asphalt mixture specimens compacted using field and laboratory methods, Constr. Build. Mater. 270 (2021) 121488. https://doi.org/10.1016/j.conbuildmat.2020.121488.
[31] D. ASTM, 448-03. Standard Classification for Sizes of Aggregate for Road and Bridge Construction, in: American Society for Testing and Materials, 2003.
[32] M., Khodadadi, L., Moradi, B., Dabir, F.M. Nejad, and A., Khodaii, Reuse of drill cuttings in hot mix asphalt mixture: A study on the environmental and structure performance. Construction and Building Materials, 256, (2020) p.119453.
[33] M., Khodadadi, F. Moghadas Nejad, and A., Khodaii. Comparison of Rut Susceptibility Parameters in Modified Bitumen with PPA. AUT Journal of Civil Engineering, 1(2), (2017), pp.129-134.
[34] A., Mahpour, M., Khodadadi, M. Shahraki, and, F., Moghadas Nejad. Evaluation of moisture durability of modified asphalt mixture with nano-titanium dioxide using surface free energy method. Amirkabir Journal of Civil Engineering, 54(8), (2022) pp.2831-2850.
[35] M., Khodadadi, A. Azarhoosh, and A., Khodaii. Influence of polymeric coating the aggregate surface on moisture damage of hot mix asphalt. Periodica Polytechnica Civil Engineering, 65(2), 2021 pp.376-384.
[36] A. Khodaii, S. Fallah, F.M. Nejad, Effects of geosynthetics on reduction of reflection cracking in asphalt overlays, Geotextiles and Geomembranes 27 (2009) 1–8.
[37] F. Moghadas Nejad, A. Noory, S. Toolabi, S. Fallah, Effect of using geosynthetics on reflective crack prevention, International Journal of Pavement Engineering 16 (2015) 477–487.
[38] K. Sobhan, V. Tandon, Mitigating reflection cracking in asphalt overlays using geosynthetic reinforcements, Road Materials and Pavement Design 9 (2008) 367–387.
[39] D. Zamora-Barraza, M.A. Calzada-Pérez, D. Castro-Fresno, A. Vega-Zamanillo, Evaluation of anti-reflective cracking systems using geosynthetics in the interlayer zone, Geotextiles and Geomembranes 29 (2011) 130–136.
[40] M. Khodadadi, A. Khodaii, J. Absi, P. Hajikarimi, F.F. Tehrani, Multi-Length-Scale Investigation of the Fatigue Behavior of Bituminous Composites: Experimental Approach, Journal of Materials in Civil Engineering 37 (2025) 4025189. https://doi.org/10.1061/JMCEE7.MTENG-19135.
[41] M. Khodadadi, A. Khodaii, P. Hajikarimi, F. Fakhari Tehrani, J. Absi, Multi-Scale Numerical Viscoelastic Simulation of Fatigue Behavior of Asphalt Mixtures Modified with Polyphosphoric Acid, IOP Conf. Ser. Mater. Sci. Eng. 416 (2018) 12106. https://doi.org/10.1088/1757-899X/416/1/012106.
[42] F.M. Nejad, S. Asadi, S. Fallah, M. Vadood, Statistical-experimental study of geosynthetics performance on reflection cracking phenomenon, Geotextiles and Geomembranes 44 (2016) 178–187. https://doi.org/10.1016/j.geotexmem.2015.09.002.
[43] M. Khodadadi, A. Khodaii, J. Absi, P. Hajikarimi, F.F. Tehrani, Multi-Length-Scale Investigation of the Fatigue Behavior of Bituminous Composites: Numerical Approach, Journal of Materials in Civil Engineering 38 (2026) 4026011. https://doi.org/10.1061/JMCEE7.MTENG-21148.
[44] H. Harkat, A.E. Ruano, M.G. Ruano, S.D. Bennani, GPR target detection using a neural network classifier designed by a multi-objective genetic algorithm, Applied Soft Computing Journal 79 (2019) 310–325. https://doi.org/10.1016/j.asoc.2019.03.030.
[45] Z. Liu, X. Gu, H. Yang, L. Wang, Y. Chen, D. Wang, Novel YOLOv3 Model With Structure and Hyperparameter Optimization for Detection of Pavement Concealed Cracks in GPR Images, IEEE Transactions on Intelligent Transportation Systems 23 (2022) 22258–22268. https://doi.org/10.1109/TITS.2022.3174626.
[46] Z. Qiu, Z. Zhao, S. Chen, J. Zeng, Y. Huang, B. Xiang, Application of an Improved YOLOv5 Algorithm in Real-Time Detection of Foreign Objects by Ground Penetrating Radar, Remote Sens. (Basel). 14 (2022). https://doi.org/10.3390/rs14081895.
[47] J. Fan, J.H. Lee, I.S. Jung, Y.K. Lee, Improvement of Object Detection Based on Faster R-CNN and YOLO, 2021 36th International Technical Conference on Circuits/Systems, Computers and Communications, ITC-CSCC 2021 (2021) 3–6. https://doi.org/10.1109/ITC-CSCC52171.2021.9501480.
[48] D. Ma, H. Fang, N. Wang, B. Xue, J. Dong, F. Wang, A real-time crack detection algorithm for pavement based on CNN with multiple feature layers, Road Materials and Pavement Design 23 (2022) 2115–2131. https://doi.org/10.1080/14680629.2021.1925578.
[49] Q. Yang, W. Shi, J. Chen, W. Lin, Deep convolution neural network-based transfer learning method for civil infrastructure crack detection, Autom. Constr. 116 (2020) 103199. https://doi.org/10.1016/j.autcon.2020.103199.
[50] M.G. Zamani, M.R. Nikoo, D. Rastad, B. Nematollahi, A comparative study of data-driven models for runoff, sediment, and nitrate forecasting, J. Environ. Manage. 341 (2023) 118006.

[51] L. Ali, F. Alnajjar, H. Al Jassmi, M. Gochoo, W. Khan, M.A. Serhani, Performance evaluation of deep CNN-based crack detection and localization techniques for concrete structures, Sensors 21 (2021) 1–22. https://doi.org/10.3390/s21051688.
[52] M., Gholami, M., Khodadadi, P., Hajikarimi, and A., Khodaii. Investigating the effects of reducing the number of temperatures and frequencies on the development of master curves for viscoelastic properties of bituminous composite. Measurement, 230, (2024), p.114503.
[53] F. Zhou, T. Scullion, L. Sun, Verification and modeling of three-stage permanent deformation behavior of asphalt mixes, J. Transp. Eng. 130 (2004) 486–494.
[54] Z. Tong, J. Gao, H. Zhang, Recognition, location, measurement, and 3D reconstruction of concealed cracks using convolutional neural networks, Constr. Build. Mater. 146 (2017) 775–787. https://doi.org/10.1016/j.conbuildmat.2017.04.097.